J O U R N A L O F
Ceramic
Processing Research

Citric acid stabilized iron oxide nanoparticles for battery-type supercapacitor electrode

Seungil Park[a], C. Justin Raj[a], Ramu Manikandan[b], Byung Chul Kim[b] and Kook Hyun Yu[a],*
[a]*Department of Chemistry, Dongguk University, Jung-gu, Seoul-04620, Republic of Korea*
[b]*Department of Printed Electronics Engineering, Sunchon National University, 255, Jungang-ro, Suncheon-si, Jellanamdo 57922, Republic of Korea*

We report the synthesis of citrate stabilized iron oxide (C-Fe$_3$O$_4$) spherical nanoparticles for supercapacitor electrodes. The citrate functional group present in the surface of the Fe$_3$O$_4$ nanoparticles effectively controls the morphology and the surface area of the nanostructures. The C-Fe$_3$O$_4$ electrodes exhibited a battery-like energy storage properties with a maximum specific capacity of 146 Cg^{-1} (242 Fg^{-1}) which is much higher than the specific capacity of citrate free Fe$_3$O$_4$ electrode (62 Cg^{-1}; 112 Fg^{-1}). Moreover, the C-Fe$_3$O$_4$ electrode showed better cyclic stability (75%) than the citrate free Fe$_3$O$_4$ electrode (~35%) after 1000 charge/discharge cycles.

Keywords: Ion oxide, Nanoparticle, Supercapacitor.

Introduction

Transitional metal oxides (TMOs) are the potential pseudocapacitive electrode materials as they have multiple valence states of the metal ions that could enable a fast-faradaic redox reaction near to the surface region. In the recent past, a variety of TMOs such as RuO$_2$, MnO$_2$, Co$_3$O$_4$, NiO, Fe$_3$O$_4$ was studied for their capacitive performance [13]. Among all these transition metal oxides, iron oxides exhibit considerable attractions due to their low toxicity, natural abundance, low cost, environmental friendliness and rich redox chemistry and having multiple applications due to their unique structural, electrical and magnetic properties [4, 5]. Generally, iron oxides are promising negative electrode materials for supercapacitors owing to its excellent electrochemical performance in the negative potential window with a high theoretical capacitance [6]. However, few researchers have been reported Fe$_3$O$_4$ as a positive electrode material and displayed considerable electrochemical performances which are even comparable or higher than the well-known TMOs like Co$_3$O$_4$, MnO$_2$, CuO etc., [7, 9].

In general, the metal oxides nanoparticle synthesized through conventional chemical techniques suffers from the agglomeration of nanoparticles, which significantly leads to the formation of large-sized particles with poor surface area and porosity [10]. In order to overcome this issue, the Fe$_3$O$_4$ surface should be stabilized with citric acid via the coordination bond which can be

acted as a promising catalyst for the formation of pyrimidine derivative compound. Further, high surface area of CA anchored Fe$_3$O$_4$ also plays a significant role to determine their catalytic performance [11]. As the electrochemical performance of the supercapacitor electrode highly depends upon the surface area and porous nature of the electroactive materials, it is important to control the size and modifying the porosity of the nanoparticles to provide large electroactive surface area for the effective charge-storage process.

Considering these crucial electrochemical factors, we synthesized water dispersible, citrate stabilized Fe$_3$O$_4$ nanoparticles and utilized for the fabrication of super-capacitor electrode. The citrate stabilization considerably controls the particle size, surface area and porosity of the Fe$_3$O$_4$ nanoparticles and the fabricated electrode exhibited an excellent battery-like charge storage property in the positive potential window.

Experimental

The water-dispersible citrate capped iron oxide (C-Fe$_3$O$_4$) was prepared according to the synthesis procedure reported in our previous work [12]. In brief, FeCl$_3$·6H$_2$O (0.016 mol) and FeCl$_2$·4H$_2$O (0.008 mol) were dissolved in 80 ml deionized (DI) water and reflexed for 30 min at 70 °C under argon atmosphere. Subsequently, the 20 mL of 28% ammonia solution was added slowly to the mixture until the formation of a black turbid solution. Then, 4 mL of 2.6 M citric acid solution was added to the reaction mixture and the temperature was raised to 90 °C under refluxing condition and maintained for 60 min. Finally, the mixture was

*Corresponding author:
 Tel : +82 2 2260 3709
 Fax: +82 2 2268 8204
 E-mail: yukook@dongguk.edu

cool down to the room temperature and the C-Fe$_3$O$_4$ nanoparticles were centrifuged, washed repeatedly and dispersed in DI water. The citrate free Fe$_3$O$_4$ nanoparticles were synthesized by the heat treatment of the C-Fe$_3$O$_4$ samples at 300 °C for 30 min per the TG curve (Fig. 1(a)). The FTIR spectra of the samples confirm the successful removal of citrate functional groups such as OH stretching (3,439 cm^{-1}), C=O stretching (1,602 cm^{-1}), symmetric stretching of COO$^-$ (1,400 cm^{-1}) groups from the surface of the C-Fe$_3$O$_4$ nanoparticles [13, 14] (Fig. 1(b)).

The structural properties of the synthesized samples were identified by powder X-ray diffraction (XRD, Rigaku, Ultima IV) using Ni filtered Cu Kα radiation (λ = 1.5418 Å) operated at 40 kV and 30 mA in the 2θ range 20°- 80°. Morphological study of the sample was performed utilizing transmission electron microscopy (TEM) (JEOL (Japan) model JEM-2100F). The nitrogen adsorption/desorption measurement was carried out using a Microtrac, BELsorp-mini II surface analyzer employing the volumetric method. The specific surface area was calculated by the Brunauer-Emmett-Teller (BET) technique and the pore size distribution was estimated from the desorption branch of the isotherm by the Barrett-Joyner-Halenda (BJH) method. Attenuated total reflectance - Fourier transform Infrared Spectroscopy (ATR-FTIR) measurement was performed using ATR-FTIR spectrometer (Smiths Detection).

The supercapacitor electrodes were fabricated by mixing the active materials (C-Fe$_3$O$_4$ or Fe$_3$O$_4$) (75 wt%), acetylene black (20 wt%) and polyvinylidene fluoride (5 wt%) in N-methyl-2-pyrrolidone. The obtained paste was coated over a nickel foam substrate of exposed geometric area 1×1 cm^2 and dried at 100 °C for 12 h in a vacuum oven. The mass of the active material present in the electrodes was determined ~3.5 mg. Electrochemical measurements such as cyclic voltammetry, galvanostatic charge/discharge test and impedance spectroscopy were performed at room temperature (~25 °C) using a ZIVE-SP2 (Korea) electrochemical workstation. The measurements were

carried out in a three-electrode setup consisting of a working electrode of Ni foam coated with the active material, a platinum counter electrode and a Hg/HgO reference electrode in 6M KOH aqueous electrolyte. The electrochemical impedance spectra (EIS) of the electrodes were measured in the frequency range of 10 mHz - 100 kHz at equilibrium open circuit potential 0 V with an AC perturbation of 5 mV in 6 M KOH electrolyte.

The specific capacity (Q$_s$) value of the electrodes was calculated using eq. (1).

$$Q_s = \frac{I \times \Delta t}{m} \tag{1}$$

where, I is the constant discharge current (A), Δt is the discharge time (s) and m is the mass of the active material (g) in the electrodes.

Results and Discussion

The crystal structures of synthesized samples were studied using XRD analysis as shown in Fig. 2(a). The XRD patterns show strong and broad diffraction peaks representing the formation of crystalline Fe$_3$O$_4$ nanostructures and the corresponding peaks are indexed to a face-centered cubic lattice of Fe$_3$O$_4$ (JCPDS Card No. 19-0629). From the diffraction patterns citrate free Fe$_3$O$_4$ exhibited slightly high intensity than the C-Fe$_3$O$_4$ representing the crystallinity of the sample increased on heat-treatment. The nitrogen adsorption/desorption isotherms of the samples are shown in Fig. 2(b) and the inset show the pore size distribution of the samples. The adsorption/desorption shows the samples exhibit type-IV hysteresis loop, that is characteristic of mesoporous materials. The BET surface area of the C-Fe$_3$O$_4$ sample is calculated to be 131.07 m^{2}g^{-1} and it decreased to 67.39 m^{2}g^{-1} after the heat-treatment of the sample. These decrease in BET surface area is mainly attributed to the removal of surface functionalities to form more agglomerated nanostructure. Similarly, the total pore
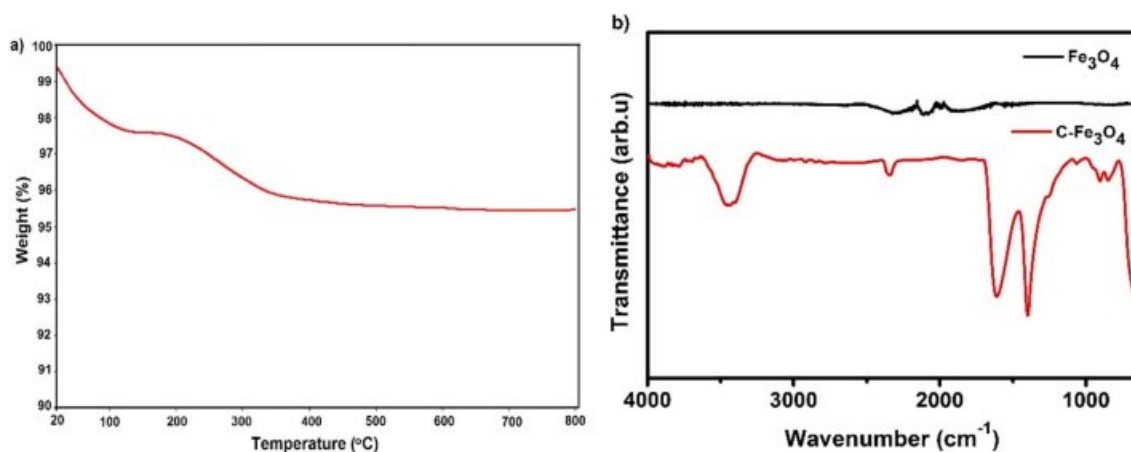

**Fig. 1.** (a) TGA curve of C-Fe$_3$O$_4$ and (b) FTIR spectrum of C-Fe$_3$O$_4$ and Fe$_3$O$_4$ samples.

volume of the sample also decreases from 0.281 to 0.224 cm^3 g^{-1} for Fe$_3$O$_4$ sample and the estimated average pore diameter of C-Fe$_3$O$_4$ and Fe$_3$O$_4$ samples are 9 nm and 13 nm respectively, which confirms the mesoporous distribution of the synthesized nanostructures. Thus, these samples can offer considerable attaching area between active materials and the electrolyte for

better electrochemical performance [15, 16].

The surface morphology of the C-Fe$_3$O$_4$ and Fe$_3$O$_4$ samples were examined by TEM analysis. Fig. 3(a) shows the TEM image of C-Fe$_3$O$_4$ and it displays well-defined spherical morphology with slightly interconnected nanoparticles of size ranges from 10-20 nm. Moreover, the sample depicts well-dispersed nature without much
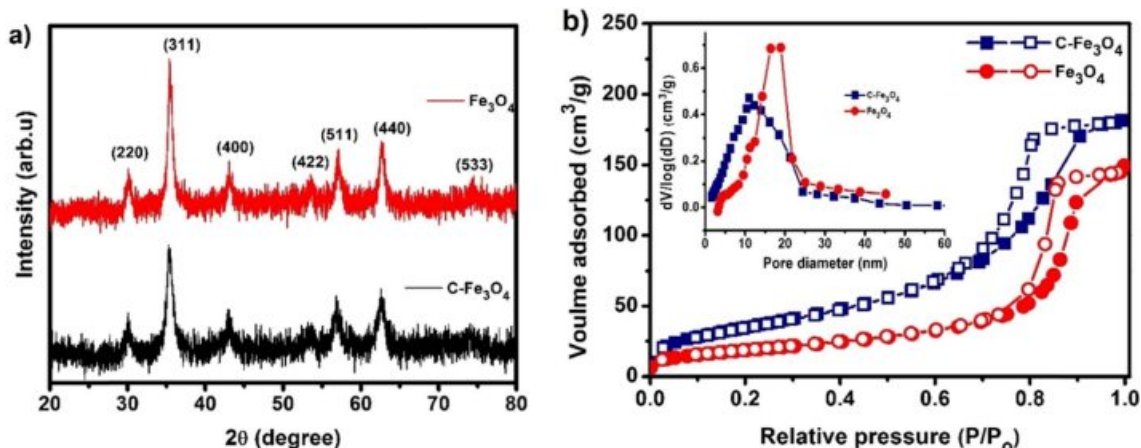
Fig. 2. (a) XRD patterns of C-Fe$_3$O$_4$ and Fe$_3$O$_4$ samples, (b) N$_2$ adsorption/desorption isotherms of the C-Fe$_3$O$_4$ and Fe$_3$O$_4$ and the inset pore size distribution of the samples.
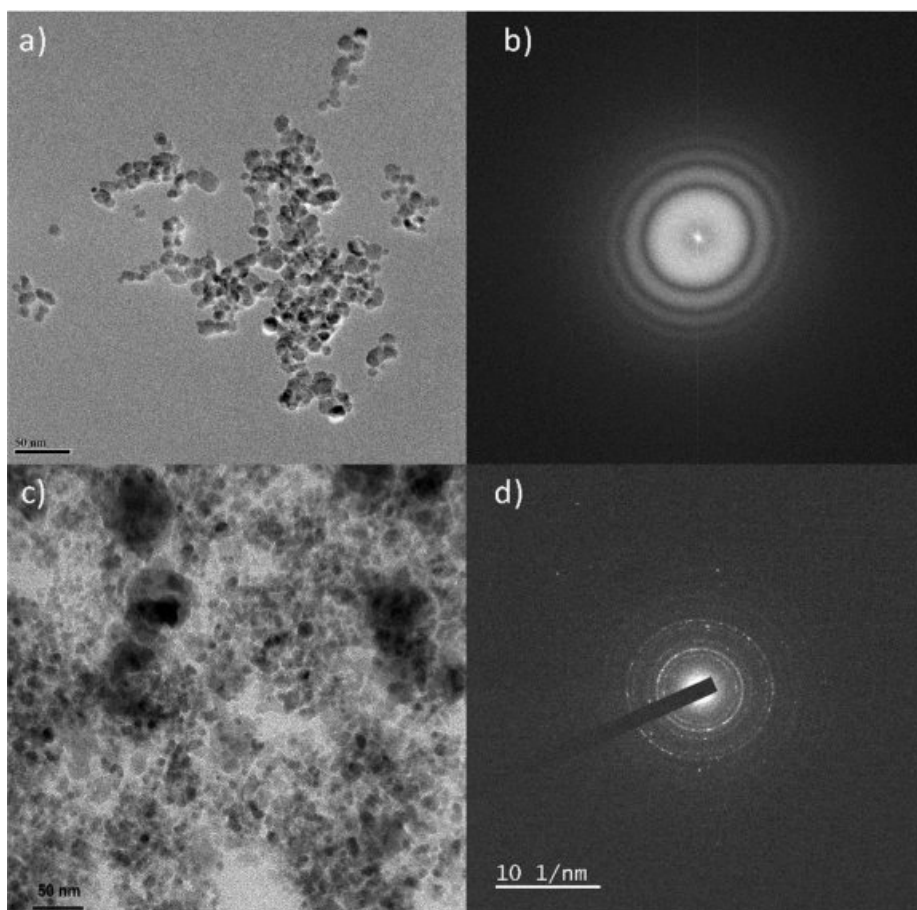

Fig. 3. (a) TEM image of C-Fe$_3$O$_4$ nanoparticles, (b) SAED pattern of the C-Fe$_3$O$_4$ nanoparticles, (c) TEM image of Fe$_3$O$_4$ nanoparticles and (d) SAED pattern of the Fe$_3$O$_4$ nanoparticles.

agglomerations of the nanoparticles. But the TEM image (Fig. 3(c)) of the heat-treated sample (Fe_3O_4) displays highly agglomerated spherical nanoparticles with few slightly big sized nanoparticles. Thus, the subsequent heat treatment and removal of surface citrate groups from the sample highly influence the size of nanoparticles. The corresponding selected area electron diffraction (SAED) pattern of C-Fe_3O_4 and Fe_3O_4 samples are shown in Fig. 3(b) and (d) respectively. As absorbed in XRD, the SAED pattern of the heat-treated sample is more crystalline than the citrate stabilized Fe_3O_4 sample.

Electrochemical capacitance performances of the C-Fe_3O_4 and Fe_3O_4 electrodes were investigated by cyclic voltammetry (CV), galvanostatic charge/discharge (GCD) test and electrochemical impedance spectroscopy (EIS) in 6M KOH electrolyte. Fig. 4(a) shows the CVs of the bare Ni-foam, C-Fe_3O_4 and Fe_3O_4 electrodes (~3.5 mg) measured at 10 mVs^{-1} scan rates. The CV of bare Ni-foam exhibited distinct pair of redox peaks originated from the Faradaic redox reaction of Ni elemental species in an alkaline electrolyte and the similar pair of redox peaks are exhibited in the C-Fe_3O_4 and Fe_3O_4 electrodes. However, the citrate free Fe_3O_4 electrode displays a secondary reduction peak with comparatively broad oxidation peak than the Ni-foam, which corresponds to the redox reaction of Fe(II)/Fe(III) redox couple of

the electrode material. The C-Fe_3O_4 electrode shows a significantly larger redox peak area represents the overlapping the two peaks observed in Fe_3O_4 electrode, moreover, the electrode exhibited high background current revealing superior capacitive performance than the other two electrodes. Moreover, these irregular shape of the CVs with redox peaks correspond the non-capacitive faradic or battery-like redox characteristic of the electrodes [17, 18]. This enhancement in C-Fe_3O_4 electrode over Fe_3O_4 is mainly due to the improved surface area and pore density of the sample due to the stabilization of citrate functional groups on the surface. Further, the CVs of the electrodes measured for various scan rates are displayed in Fig. 4(b) and (c). From these CVs, C-Fe_3O_4 electrode possesses higher background current and redox peak intensity for all the measured scan rates. Moreover, the electrodes nearly retain its shapes even at higher scan rates representing better supercapacitor electrode materials.

The GCD curves of the C-Fe_3O_4 and Fe_3O_4 electrodes at 1 Ag^{-1} specific current is shown in Fig. 4(d) and the curves display a nonlinear shape, which reveals the non-capacitive faradic reaction that typically exhibited in the supercapattery electrode materials due to the battery-type charge storage mechanism [19, 20]. Similar to CVs, the GCD curve shows a prolonged charge/discharge time for C-Fe_3O_4 electrode than Fe_3O_4 electrode
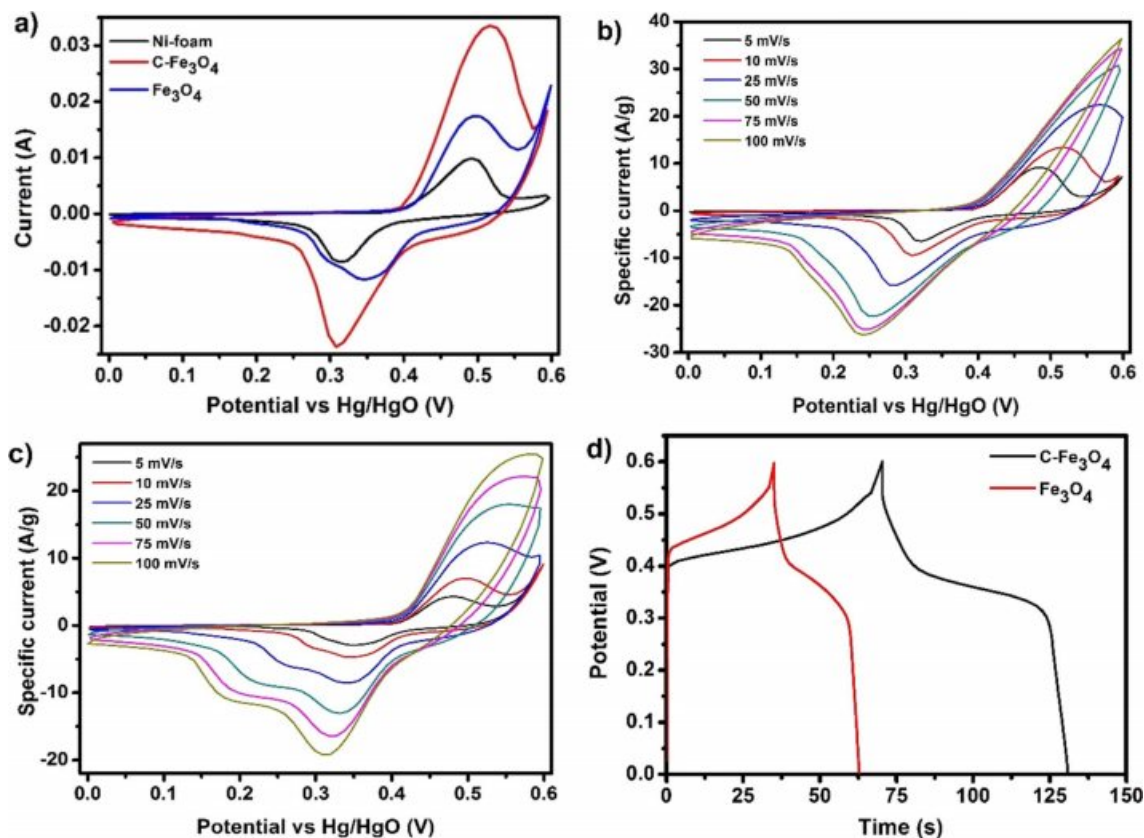
Fig. 4. (a) CVs of bare Ni-foam, C-Fe_3O_4 and Fe_3O_4 electrode at 10 mV s^{-1} scan rate, CVs of bare, (b) C-Fe_3O_4 and (c) Fe_3O_4 electrodes measured at various scan rates, and d) the GCD curves of C-Fe_3O_4 and Fe_3O_4 electrodes at 1 A g^{-1}.

representing better capacitive performance. The specific capacity (Q_s) values of the electrodes were calculated and the C-Fe$_3$O$_4$ electrode shows maximum specific capacity 146 Cg^{-1} (242 Fg^{-1}) at a specific current 1 A g^{-1}, which is much higher than the Fe$_3$O$_4$ electrode (62 Cg^{-1}; 112 Fg^{-1}).

Fig. 5(a) and (b) shows the GCD curves of C-Fe$_3$O$_4$ and Fe$_3$O$_4$ electrodes measured for various specific currents and Fig. 5(c) displays the variation of specific capacity of the electrodes for various specific currents. From this, the C-Fe$_3$O$_4$ electrode demonstrates higher specific capacity values for all the measured specific currents with relatively higher discharge time than the Fe$_3$O$_4$ electrode. Moreover, the specific capacity of the electrodes decreases with the increase in specific currents due to the increasing IR-drop and the limited involvement of active material in a redox reaction concerning the increase in specific currents [21]. Fig. 5(d) shows the cyclic stability of the C-Fe$_3$O$_4$ and Fe$_3$O$_4$ electrodes for 1,000 charge/discharge cycles at 10 Ag^{-1}. The C-Fe$_3$O$_4$ electrode shows comparable cyclic stability with ~75% of the specific capacity retention after 1,000 cycles. But, the Fe$_3$O$_4$ electrode displays only ~35% specific capacity retention representing nearly poor stability of the electrode.

The Nyquist plots of the electrodes are shown in Fig. 6(a) and the inset shows the magnified portion of the high-frequency region of the plots. The Nyquist plots were fitted using Zview software with an equivalent circuit (inset of Fig. 6(a). The circuit consists of a bulk resistance (R_s) [11, 22, 23] and a parallel combination of resistance R_{ct} and capacitance (C_{dl}) represents the charge-transfer resistance and electric double layer capacitance contribution of the electrodes. The slight inclined low-frequency slope was fitted with the Warburg element (W_s) corresponding the diffusion control process of the electrodes. Additional constant phase elements CPE$_1$ included in the circuit due to the non-ideal capacitive behavior of the electrodes and it represents the energy storage process originated from the redox reaction [24]. The best-fitted results of the electrodes are presented in Table.1. From these, the R$_s$ value of the electrodes found to be nearly similar, but the charge transfers resistance R_{ct} value of C-Fe$_3$O$_4$ electrode lower than the Fe$_3$O$_4$ electrode. This is mainly attributed to high mesoporosity of the electrode materials may account these better charge-transfer process than the Fe$_3$O$_4$ electrode [25]. Fig. 6(b) shows the corresponding Bode phase plots of electrodes with low frequency (100 mHz) phase angle of -76.5 and 55°. The existence of high phase angle at low frequency (approaches slightly close to the ideal capacitor, -90°) for C-Fe$_3$O$_4$ electrode denotes the better charge storage properties of the electrode than the citrate free Fe$_3$O$_4$ electrodes [26].
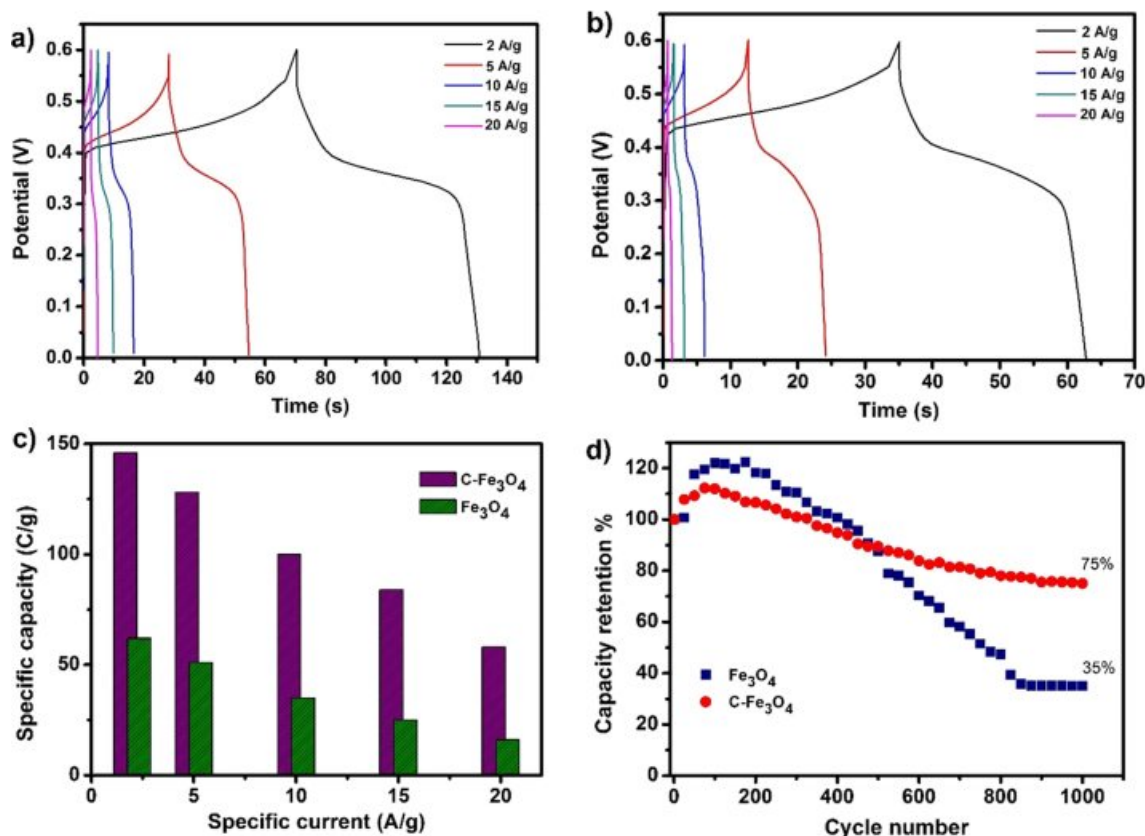
Fig. 5. Charge/discharge curves of (a) C-Fe$_3$O$_4$ and (b) Fe$_3$O$_4$ electrodes for different specific currents, (c) Variation of specific capacity with various specific currents and (e) Cyclic stability of the electrodes for 1,000 cycles at 10 Ag^{-1}.
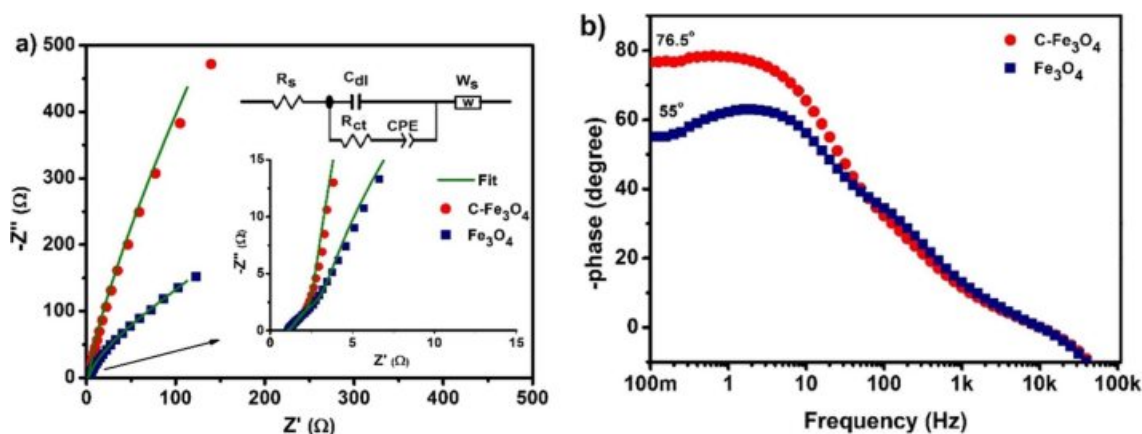
Fig. 6. (a) Nyquist plots (the inset shows a magnified part and equivalent circuit) and b) Bode plots of the C-Fe$_3$O$_4$ and Fe$_3$O$_4$ electrodes

Table 1. EIS fitted parameters of C-Fe$_3$O$_4$ and Fe$_3$O$_4$ electrodes.

Samples	R_s (Ω cm^2)	R_{ct} (Ω cm^2)	W_R (Ω cm^2)	C_{dl} (mF cm^{-2})	CPE$_2$ (mF cm^{-2})
C-Fe$_3$O$_4$	1.07	3.43	1.47	1.26	2.21
Fe$_3$O$_4$	1.01	5.32	2.21	0.56	2.61

Conclusion

In summary, the synthesized citrate stabilized iron oxide nanoparticles possess a controlled size, mesoporosity and high surface area than the citrate free Fe$_3$O$_4$ nanoparticles. These improved properties demonstrate the C-Fe$_3$O$_4$ nanoparticles as a promising supercapacitor electrode material with a battery like a charge storage behavior and excellent electrochemical performances.

Acknowledgements

References

1. W. Deng, X. Ji, Q. Chen, C.E. Banks, RSC Adv. 1 (2011) 1171-1178.
2. M.Y. Cho, S.M. Park, B. H. Choi, J.-W. Lee, K. C. Roh, J. Ceram. Process. Res. 13(S2) (2012) 166-169.
3. D. Qiu, X. Ma, J. Zhang, B. Zhao, Z. Lin, Chem. Phys. Lett. 710 (2018) 188-192.
4. M.P. Kumar, L.M. Lathika, A.P. Mohanachandran, R.B. Rakhi, ChemistrySelect 3 (2018) 3234-3240.
5. G.V.M. Williams, T. Prakash, J. Kennedy, S.V. Chong, S. Rubanov, J. Magn. Magn. Mater. 460 (2018) 229-233.
6. V.D. Nithya, N. Sabari Arul, J. Mater. Chem. A 4 (2016) 10767-10778.
7. S. Mallick, P.P. Jana, C.R. Raj, Chem. Electro. Chem. 5 (2018) 2348-2356.
8. L. Song, Y. Han, F. Guo, Y. Jiao, Y. Li, Y. Liu, F. Gao, J. Nanomater. 2018 (2018) 1-13.
9. F. Yang, X. Zhang, Y. Yang, S. Hao, L. Cui, Chem. Phys. Lett. 691 (2018) 366-372.
10. M. Aghazadeh, I. Karimzadeh, M. Reza Ganjali, Mater. Lett. 209 (2017) 450-454.
11. L. Li, C. Polanco, A. Ghahreman, J. Electroanal. Chem. 774 (2016) 66-75.
12. B.-B. Cho, J.H. Park, S.J. Jung, J. Lee, J.H. Lee, M.G. Hur, C. J. Raj, K.-H. Yu, J. Radioanal. Nucl. Chem. 305 (2015) 169-178.
13. C. Hui, C. Shen, T. Yang, L. Bao, J. Tian, H. Ding, C. Li, H.-J. Gao, J. Phys. Chem. C 112 (2008) 11336-11339.
14. S. Nigam, K.C. Barick, D. Bahadur, J. Magn. Magn. Mater. 323 (2011) 237-243.
15. J. Yao, Y. Gong, S. Yang, P. Xiao, Y. Zhang, K. Keyshar, G. Ye, S. Ozden, R. Vajtai, P.M. Ajayan, ACS Appl. Mater. Interfaces 6 (2014) 20414-20422.
16. Z. Gu, H. Nan, B. Geng, X. Zhang, J. Mater. Chem. A 3 (2015) 12069-12075.
17. N. Padmanathan, H. Shao, D. McNulty, C. O'Dwyer, K.M. Razeeb, J. Mater. Chem. A 4 (2016) 4820-4830.
18. B.C. Kim, R. Manikandan, K.H. Yu, M.-S. Park, D.-W. Kim, S.Y. Park, C. J. Raj, J. Alloys Compnd. 789 (2019) 256-265.
19. H. Chen, S. Chen, Y. Zhu, C. Li, M. Fan, D. Chen, C. Tian, K. Shu, Electrochim. Acta 190 (2016) 57-63.
20. N. Tang, H. You, M. Li, G.Z. Chen, L. Zhang, Nanoscale 10 (2018) 20526-20532.
21. R. Manikandan, C. J. Raj, M. Rajesh, B.C. Kim, G. Nagaraju, W.-G. Lee, K.H. Yu, J. Mater. Chem. A 6 (2018) 11390-11404.
22. S.H. Lee, J.M. Kim, J.R. Yoon, J. Ceram. Process. Res. 18 (2017) 51-54.
23. C.J. Raj, M. Rajesh, R. Manikandan, J.Y. Sim, K.H. Yu, S.Y. Park, J.H. Song, B.C. Kim, Electrochim. Acta 247 (2017) 949-957.
24. F.B. Ajdari, E. Kowsari, A. Ehsani, M. Schorowski, T. Ameri, Electrochim. Acta 292 (2018) 789-804.
25. H. Liu, P. He, Z. Li, Y. Liu, J. Li, Electrochimica Acta 51 (2006) 1925-1931.
26. X. Pan, G. Ren, M.N.F. Hoque, S. Bayne, K. Zhu, Z. Fan, Adv. Mater. Interfaces 1 (2014) 1400398.